

Cite this: *J. Mater. Chem.*, 2012, **22**, 19744

www.rsc.org/materials

PAPER

Induction of the surface plasmon resonance from C-incorporated Au catalyst in  $\text{Si}_{1-x}\text{C}_x$  nanowires†Woo-Jung Lee,<sup>a</sup> Jin Won Ma,<sup>a</sup> Jung Min Bae,<sup>a</sup> Sang Han Park,<sup>a</sup> Kwang-Sik Jeong,<sup>a</sup> Mann-Ho Cho,<sup>\*a</sup> Chul Lee,<sup>b</sup> Kyong-Joo Han<sup>c</sup> and Kwun-Bum Jeong<sup>c</sup>

Received 1st June 2012, Accepted 30th July 2012

DOI: 10.1039/c2jm33527a

$\text{Si}_{1-x}\text{C}_x$  nanowires (NWs) were synthesized by varying the ratio of  $\text{SiH}_4$  and  $\text{CH}_3\text{SiH}_3$  gases using a vapor–liquid–solid (VLS) procedure using Au as a catalyst. The growth rate of the  $\text{Si}_{1-x}\text{C}_x$  NWs and the change in the wire shape from straight to helical near the Au tip were found to be closely related to the ratio of the  $\text{CH}_3\text{SiH}_3$  content. The large concentration of C in the  $\text{Si}_{1-x}\text{C}_x$  NWs was proportional to the  $\text{CH}_3\text{SiH}_3$  content, overcoming the extremely low solubility of C in Si, resulting in an interstitial incorporation of C atoms in the wire. This incorporation can be attributed to the cleavage of Si–C bonds in the  $\text{CH}_3\text{SiH}_3$  compound through the Au catalyst (an Au–Si liquid-state cluster of about 70–100 nm) during wire growth by the VLS method. Simultaneously supplying  $\text{CH}_3\text{SiH}_3$  and  $\text{SiH}_4$  gases enhanced the diffusion of Au atoms from the tip to the sidewall of the wire, while also deforming the shape of the Au tip. When the  $\text{CH}_3\text{SiH}_3$  gas was increased to 1.5 sccm, the number of Au nanoparticles (2–3 nm in size) at the lateral surface induced a surface plasmon resonance (SPR) and improved the optical conductivity ( $\sigma$ ) of the  $\text{Si}_{1-x}\text{C}_x$  NWs. For 2 sccm of  $\text{CH}_3\text{SiH}_3$ , a remarkable increase in the number of C atoms incorporated in the Au nanoparticles along the sidewall red shifted the SPR peak, suggesting that the SPR can be modulated by the Au–C interactions in the nanoparticles.

## I. Introduction

As a component of nearly ten million different compounds, carbon is an abundant and intriguing element. More specifically, carbon-containing group-IV semiconductor alloys such as  $\text{Si}_{1-x}\text{C}_x$  and  $\text{Si}_{1-x-y}\text{Ge}_y\text{C}_y$  have been the subject of considerable attention, particularly owing to the potential they offer for band engineering *via* strain control in microelectronic and optoelectronic devices.<sup>1,2</sup> According to literature reports, Si–C alloy systems show several physical characteristics – *e.g.*, a substantial lattice mismatch between Si and C (~52%), a very low equilibrium solid solubility in Si ( $10^{-4}$  at% at 1400 °C), and a tendency to form precipitates comprising SiC microcrystallites to lower their energy at higher temperatures ( $\leq 950$  °C).<sup>3–5</sup> Although extensive studies have examined the increase in the substitutional C content in bulk Si, the complete incorporation of C into substitutional sites in  $\text{Si}_{1-x}\text{C}_x$  films occurs at C concentrations of only up to ~2 at% and only over very narrow growth conditions, due to the extremely low solubility of C in Si.<sup>6–9</sup> Furthermore, while the above-mentioned characteristics of Si–C systems have

been verified in two-dimensional  $\text{Si}_{1-x}\text{C}_x$  film growth, methods for preparing and analyzing  $\text{Si}_{1-x}\text{C}_x$  nanostructures with filamentous configurations (*e.g.*, nanowires) have been thoroughly developed only for SiC NWs. In this paper, we introduce the first mechanistic study of  $\text{Si}_{1-x}\text{C}_x$  NWs grown using a VLS method with Au as the catalyst. Among the various C precursor gases, such as  $\text{C}_3\text{H}_8$ ,  $\text{CH}_4$ ,  $\text{CH}_3\text{SiH}_3$ ,  $\text{C}(\text{SiH}_3)_4$  and  $\text{C}(\text{SiH}_2\text{Cl})_4$ , employing  $\text{CH}_3\text{SiH}_3$  for  $\text{Si}_{1-x}\text{C}_x$  film growth is of particular interest since it is the simplest organosilicon that can be used in its gas phase at room temperature and that contains no C–C bonds.<sup>5,8–13</sup> Thus, we chose  $\text{CH}_3\text{SiH}_3$  gas as the C precursor and  $\text{SiH}_4$  gas as the Si precursor for the growth of  $\text{Si}_{1-x}\text{C}_x$  NWs. In previous studies, we grew Si NWs by varying the process parameters and found the critical condition for vertical growth. The vertically grown Si NWs were then utilized as references (as shown in Fig. 1(a)) in this experiment. Interestingly, these Si NWs possess a considerable number of Au nanoparticles (with sizes of 2–3 nm) along the lateral wire surface due to the diffusion of Au atoms from the tip during wire growth. In the past decade, these metallic nanoparticles have attracted much attention because of their unique electronic, optical, and magnetic properties that vary with the particle size.<sup>14–16</sup> In particular, the surface plasmons of Au nanoparticles, induced by coherent oscillation of the conduction band electrons, have inspired a new field of research called *plasmonics*. In our system, there are two types of Au particles; one type emanates from the Au tip about

<sup>a</sup>Department of Physics and Applied Physics, Yonsei University, Seoul 120-749, Korea. E-mail: mh.cho@yonsei.ac.kr<sup>b</sup>Department of Physics, University of Seoul, Seoul 130-743, Korea<sup>c</sup>Department of Physics, Dankook University, Cheonan, 330-714, Korea

† Electronic supplementary information (ESI) available. See DOI: 10.1039/c2jm33527a

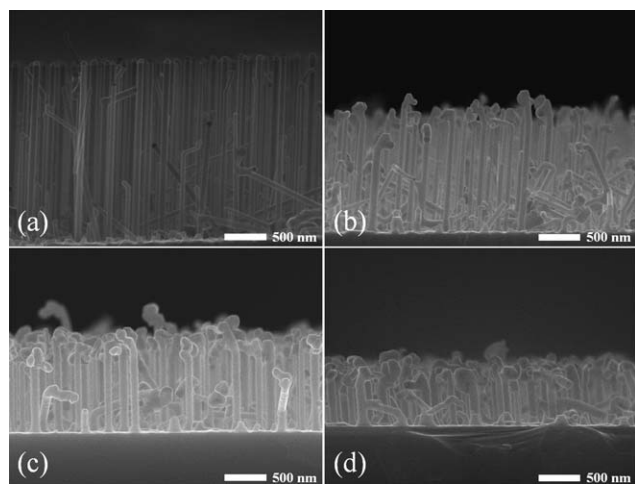


**Fig. 1** FE-SEM images of  $\text{Si}_{1-x}\text{C}_x$  NWs grown as a function of the ratio of the gas flow rates of  $\text{SiH}_4$  to  $\text{CH}_3\text{SiH}_3$ , keeping other process parameters constant. (a)  $\text{SiH}_4 : \text{CH}_3\text{SiH}_3 = 10 : 0$  sccm, (b)  $\text{SiH}_4 : \text{CH}_3\text{SiH}_3 = 10 : 1$  sccm, (c)  $\text{SiH}_4 : \text{CH}_3\text{SiH}_3 = 10 : 1.5$  sccm, and (d)  $\text{SiH}_4 : \text{CH}_3\text{SiH}_3 = 10 : 2$  sccm.

70–100 nm at the top of the wire, and the other is an Au nanoparticle about 2–3 nm in diameter, which is distributed only along the external surfaces. The existence of these two types of Au particles fosters various interesting and exotic phenomena in the growth of  $\text{Si}_{1-x}\text{C}_x$  NWs, including the following: (i) a large amount of C ( $\sim 12$  at% in 2 sccm of  $\text{CH}_3\text{SiH}_3$ ), which can be incorporated into the wires *via* the Au tip, despite a very low solid solubility of C in Si (surprisingly, this factor has not yet been investigated in  $\text{Si}_{1-x}\text{C}_x$  films); (ii) a decreasing wire growth rate with an increasing  $\text{CH}_3\text{SiH}_3$  gas flow rate; and (iii) a greater number of Au nanoparticles along the sidewall corresponding to a more deformed Au tip, in proportion to the  $\text{CH}_3\text{SiH}_3$  gas.

In order to investigate such novel features in  $\text{Si}_{1-x}\text{C}_x$  nanostructures, we analyzed their electronic and optical properties using X-ray photoemission spectroscopy (XPS) and ultraviolet-visible (UV-vis) spectroscopy, respectively. In the former, we verified that a large number of C atoms exist in the interstitial incorporation into Si lattices and chemically react with Au nanoparticles, forming Au–C bonds. In the latter, the optical conductivity ( $\sigma$ ) of  $\text{Si}_{1-x}\text{C}_x$  NWs for 1.5 sccm of  $\text{CH}_3\text{SiH}_3$  was improved, which is caused by the surface plasmon resonance (SPR) due to a certain quantity of Au nanoparticles. Our result is the first to report on the generation of the SPR from the Au nanoparticles decorated on a Si nanostructure and to suggest modulation of the SPR *via* Au–C interactions.

## II. Experimental

For this study,  $\text{Si}_{1-x}\text{C}_x$  NWs were synthesized according to the VLS method using an ultrahigh vacuum chemical vapor deposition (CVD) system. A 2 nm-thick Au film (as a catalyst) was deposited onto a cleaned Si (111) substrate in a metal growing chamber at a growth pressure of  $\sim 5 \times 10^{-7}$  Torr (deposition rate:  $0.08 \text{ \AA s}^{-1}$ ) by thermal evaporation. The sample was transferred *in-situ* to the main chamber and then annealed at a pressure of  $\sim 1 \times 10^{-8}$  Torr for 5 min at  $600^\circ\text{C}$ , which is the same

as the growth temperature, resulting in the formation of Au–Si alloy droplets from the Au film and the Si substrate.<sup>17</sup> After the formation of these droplets,  $\text{Si}_{1-x}\text{C}_x$  NWs were grown within a period of 30 min by filling the main chamber with a mixture of  $\text{SiH}_4$  and  $\text{CH}_3\text{SiH}_3$  precursors and  $\text{H}_2$  carrier gas, maintaining a fixed total pressure of 0.05 Torr *via* a feedback system with a throttle valve and a Baratron gauge. In our system, the critical condition for vertically grown Si NWs – *i.e.*, a process pressure of 0.05 Torr at  $600^\circ\text{C}$  – was adopted for the C doping system. In order to adjust the dopant concentration of C in the Si pillar, the  $\text{SiH}_4 : \text{CH}_3\text{SiH}_3$  gas ratio was varied between 10 : 0, 10 : 1, 10 : 1.5, and 10 : 2 under a fixed  $\text{H}_2$  gas flow rate of 200 sccm. Then, the morphological characteristics and crystalline structures of  $\text{Si}_{1-x}\text{C}_x$  NWs as a function of the  $\text{CH}_3\text{SiH}_3$  gas ratio were investigated using a field emission scanning electron microscope (FE-SEM, JSM 6500F, Jeol) and a transmission electron microscope (TEM) (Tecnai F20), functioning in both the high-resolution (HR-TEM) and scanning (STEM) modes at 200 kV. High-angle annular dark field (HAADF) STEM images and energy dispersive X-ray (EDX) analysis confirmed the chemical composition of the  $\text{Si}_{1-x}\text{C}_x$  NWs. To investigate the concentration of dopant atoms and chemical states in the specimen near-surface region, XPS was employed with Al  $K\alpha$  radiation (PHI-5000 Versaprobe, ULVAC-PHI Inc., Osaka, Japan). The depth profiling experiments were also carried out by means of Ne ion sputtering with an energy of 2 keV in order to determine the C distribution and the chemical state in the  $\text{Si}_{1-x}\text{C}_x$  NWs along the core direction. The pressure of the Ne source during sputtering was  $\sim 4 \times 10^{-5}$  Torr. At every stage of the profiling, narrow scans of C 1s, O 1s, Si 2p and Au 4f core level spectra were recorded. Then their atomic concentrations were calculated from the peak intensities using empirically derived atomic sensitivity factors, which were obtained by software (Multipak version 9.1.0.9, Ulvac-phi, Inc). Finally, to investigate the optical properties of the specimens, the reflectance spectra were obtained using a grating spectrometer (Cary 5) for wavelengths between 200 and 800 nm.

## III. Results and discussion

Changes in the structural shape of  $\text{Si}_{1-x}\text{C}_x$  NWs as a function of the  $\text{CH}_3\text{SiH}_3$  gas flow rate were investigated using FE-SEM, as shown in Fig. 1(a)–(d). Surprisingly, the wire length significantly decreased and the wire shape became helically distorted near the Au tip in proportion to  $\text{CH}_3\text{SiH}_3$  gas flow rates. In order to investigate the effect of  $\text{CH}_3\text{SiH}_3$  gas on the growth kinetics, we observed the changes in the morphological shape of each wire in more detail using TEM [refer to ESI Fig. S1†]. As-grown Si NWs without  $\text{CH}_3\text{SiH}_3$  gas showed straight sidewalls, and the Au tip at top of the wire was a complete hemisphere. On the other hand, when  $\text{CH}_3\text{SiH}_3$  gas was introduced, the wire bent and twisted in on itself. Its growth rate also gradually decreased with the increasing  $\text{CH}_3\text{SiH}_3$  gas flow rate. Eventually, the growth of  $\text{Si}_{1-x}\text{C}_x$  NWs was completely inhibited for high  $\text{CH}_3\text{SiH}_3$  gas contents of more than 2.5 sccm (data not shown here). In addition, as the quantity of injected  $\text{CH}_3\text{SiH}_3$  gas increased, the wire diameter and Au tip size increased as well. This feature appears to be closely related to the VLS growth mechanism with respect to the partial pressure of the precursors, as has been reported in

our previous studies.<sup>17–19</sup> In the VLS method, the growth rate is determined by the incorporation of a source gas into Au droplets and the nucleation of Si atoms at the interface between the liquid (Au–Si alloy) and the solid (Si substrate at the initial state and Si wire in the intermediate state). However, the relatively low SiH<sub>4</sub> partial pressure due to the presence of CH<sub>3</sub>SiH<sub>3</sub> gas causes the incorporation of Si into Au to diminish, while the Ostwald ripening process of Au atoms on the substrate is enhanced, resulting in a larger Au tip and wire diameter, as clearly demonstrated in Fig. S1.† Furthermore, the hemispherical shape of the Au tip changes form, which is also dependent on the increase of the CH<sub>3</sub>SiH<sub>3</sub> gas concentration. In other words, liquid-state Au atoms energetically favor the formation of clusters with hemisphere; however, introducing the CH<sub>3</sub>SiH<sub>3</sub> gas along with the SiH<sub>4</sub> gas deforms the Au tip shape, as shown in Fig. S1(b)–(d).† Data on the average diameter and length of the wire are summarized in Table 1.

We examined the configuration and crystal structure of the twisted region of the wire in detail using HR-TEM. Fig. 2(a) shows the straight sidewall of the as-grown Si NWs without CH<sub>3</sub>SiH<sub>3</sub> gas. We observed substantial black points in the vertically grown Si NWs: the points were caused by the formation of Au nanoparticles (2–3 nm in size) that were located on the outside surface of the nanowire due to the low solubility of Au in Si.<sup>18</sup> The formation of Au nanoparticles on the sidewall of the Si NWs can be attributed to the diffusion of Au atoms from the Au tip at top of the wire. The quantity of diffused Au atoms increased, in particular, at the twisted and bent regions, as evidenced by the HAADF STEM images in Fig. 2(d), where the white color denotes Au atoms. Note that as the CH<sub>3</sub>SiH<sub>3</sub> gas flow rate was gradually increased, the number of Au nanoparticles on the lateral surface increased, significantly for 1.5 sccm of CH<sub>3</sub>SiH<sub>3</sub>, shown in Fig. 2(d), especially compared to the as-grown Si NWs shown in Fig. 2(b). Moreover, after introducing the CH<sub>3</sub>SiH<sub>3</sub> gas, a faceting phenomenon on the sidewall of the wire became clearly evident, as shown in Fig. 2(c), and the number of dislocation lines connected to the faceting region increased, causing the wire shape to change from a pillar to a more twisted strand. Additionally, when 2 sccm of CH<sub>3</sub>SiH<sub>3</sub> gas was injected, sporadically deposited island layers were observed on the sidewalls of the wires, as shown in Fig. 2(e). Multiform island shapes grew on the sidewalls of the entire wires, exhibiting either an amorphous or polycrystalline structure, as evidenced by the HR-TEM images and fast Fourier transform (FFT) images of the red circle region in the inset of Fig. 2(e). According to previously reported results, the tendency of three-dimensional island nucleation depends on the interface and surface free energy as a function of the strain, and can be enhanced during the

formation of C or SiC particles. These results suggest that the growth of the island layers was induced by the introduction of a high 2 sccm CH<sub>3</sub>SiH<sub>3</sub> gas flow rate.<sup>20</sup> Under this condition, Au nanoparticles were clearly observable at the lateral surface, as were oblique multi-line planar defects, as shown in Fig. 2(f). The former is due to the condensation of diffused Au atoms on the sidewall, induced by the surface tension along the interface between the liquid and solid states. The latter can be attributed to the distortion of the crystal structure due to the injection of CH<sub>3</sub>SiH<sub>3</sub> gas, resulting in a twisted deformation. The various defects have been occasionally observed in SiC thin films with a high C concentration by several groups.<sup>20–24</sup> In our system, many twin defects are apparent in the FFT images in the inset of Fig. 2(f), which is a {111} twinning plane that has been commonly observed in as-grown Si NWs.<sup>17</sup> Thus, the significantly increased twin defects appeared in response to the distortion of the crystalline Si structure due to the incorporation of C into the wire. Despite the formation of these defects, the lattice distance in the wire remained almost identical to that between Si–Si of an FCC phase [for more detailed information on the FFT images of defects, refer to ESI Fig. S2†]. Hence, the defects were generated by the incorporation of C in the wire, while the lattice distance between Si–Si in the wire remained unchanged.

In order to investigate the incorporation of C in Si NWs, we considered various detection techniques. Conventionally, the elemental concentration in one-dimensional nanostructures is verified by EDX analysis of the HAADF STEM mode images. However, in our case, this technique was limited to determining the C concentration because whether carbon is incorporated inside the wire or not, is still an open question, due to the fact that contaminant carbon is always present in the TEM chamber or the wire surface during EDX measurements. Hence, we employed XPS as an alternative methodology, since it is known to be effective at identifying not only the chemical states but also the relative concentrations from peak positions (binding energy) and peak areas, respectively. The XPS spectra for each core-level of Si 2p, C 1s, Au 4f, and O 1s obtained from the wires grown as a function of CH<sub>3</sub>SiH<sub>3</sub> gas flow rate are shown in ESI Fig. S3.† Among all the XPS spectra, the series of C 1s spectra showed a noticeable change in the peak at ~282 eV with increasing CH<sub>3</sub>SiH<sub>3</sub> gas, as denoted by the yellow elliptical symbols in Fig. S3(b).† In general, a peak at 284.5 eV corresponds to a carbonaceous contamination or weakly bound carbon which appears consistently in XPS spectra.<sup>25</sup> On the other hand, the peak near ~282 eV can be assigned to a Si–C bonding formed by substitutional C atoms (according to reports, it appears mainly in the 282.4–283 eV region).<sup>26,27</sup> To differentiate the species of C atoms (Si–C bonding) from external contamination, we performed Ne ion sputtering on the wire at 2 kV. The sputtering process using Ne ions effectively removes surface C atoms, minimizing the damage or structural deformation of the sample.<sup>28</sup> Hence, as the sputtering process removed the native oxide, the concentration of weakly bound C atoms at the surface, located at 284.5 eV, gradually diminished. More detailed descriptions and explanations of the sputtering results of XPS are provided in ESI Fig. S4.† In clear contrast to the peak at 284.5 eV, the intensity of the C signal at ~282 eV was maintained, despite sputtering for 35 min. Based on the remaining peak at

**Table 1** Summary of the characteristics of the Si<sub>1–x</sub>C<sub>x</sub> NWs related to the average wire diameter and length as a function of the inlet gas ratio

SiH <sub>4</sub> : H <sub>2</sub> : CH <sub>3</sub> SiH <sub>3</sub> flow rate ratio (sccm)	Average diameter (nm)	Average length for 30 min (μm)
10 : 200 : 0	78 (±15.4)	2.50 (±12.5)
10 : 200 : 1	79 (±13.2)	1.67 (±8.35)
10 : 200 : 1.5	95 (±15.6)	1.33 (±6.65)
10 : 200 : 2	95 (±15.1)	0.83 (±4.15)



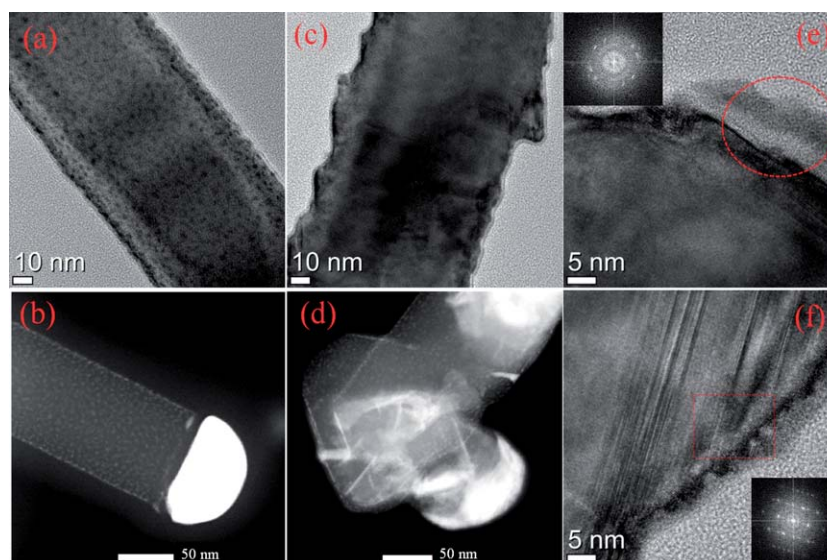
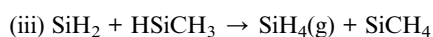
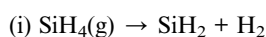


**Fig. 2** HR-TEM images and HAADF STEM images of  $\text{Si}_{1-x}\text{C}_x$  NWs grown using various  $\text{SiH}_4$  to  $\text{CH}_3\text{SiH}_3$  gas flow rate ratios. (a and b) As-grown Si NWs with straight sidewalls. (c and d) The gas flow ratio of  $\text{SiH}_4$  to  $\text{CH}_3\text{SiH}_3$  of the nanowires ranged from 10 sccm to 1.5 sccm. (e and f) The gas flow ratio of  $\text{SiH}_4$  to  $\text{CH}_3\text{SiH}_3$  of the nanowires ranged from 10 sccm to 2.0 sccm. Insets of (e) and (f) present FFT images of the regions represented by a red circle and a red rectangle, respectively. The former shows a three-dimensional growth region mixed with polycrystalline and amorphous structures. The latter reveals the twin defects generally observed in Si NWs.

$\sim 282$  eV and the change in the peak height with the  $\text{CH}_3\text{SiH}_3$  gas flow rate, we propose that C atoms were incorporated into the wire grown with  $\text{CH}_3\text{SiH}_3$  gas. In particular, the appreciable C concentrations of  $\sim 4\%$  at 1 sccm and  $\sim 13\%$  at 2 sccm are remarkably large quantities, especially considering the extremely small equilibrium solubility of C in Si at the growth temperature of  $600^\circ\text{C}$ . To verify the electronic structure of the incorporated C atoms, we carried out Raman and FT-IR measurements. Regardless of the presence of  $\text{CH}_3\text{SiH}_3$  gas, both the Raman and FT-IR spectra showed only peaks assigned to Si-Si bonding, not Si-C bonding, indicating that the features on the substitutional C atoms or Si-C bonding were not formed in the  $\text{Si}_{1-x}\text{C}_x$  NWs (this information is presented in ESI Fig. S5†).

In order to determine the number of C atoms that were incorporated into the wires, we considered the basic mechanisms of adsorption, decomposition, and desorption of the precursors during wire growth. The chemical states confirmed by XPS in Fig. S3 and S4† contain critical information related to the reaction mechanisms between Au and the precursors. The main difference between the  $\text{Si}_{1-x}\text{C}_x$  film and the  $\text{Si}_{1-x}\text{C}_x$  wire is the existence of Au as a catalyst – *i.e.*, the Au catalyst is an important factor that inhibits the chemical state of C from bonding with Si atoms. In the case of  $\text{Si}_{1-x}\text{C}_x$  film growth without the Au catalyst, C atoms can be substitutionally incorporated into Si sites with connecting Si-C bonds because the  $\text{CH}_3\text{SiH}_3$  precursor maintains its Si-C bonds at temperatures below  $600^\circ\text{C}$ .<sup>29,30</sup> The following thermal decomposition mechanisms are generally invoked for explaining  $\text{Si}_{1-x}\text{C}_x$  film growth using  $\text{SiH}_4$  and  $\text{CH}_3\text{SiH}_3$ :



The major decomposition pathway of  $\text{CH}_3\text{SiH}_3$  gas (step (ii)) shows that highly reactive intermediates of the isomeric species of  $\text{HSiCH}_3$  and  $\text{H}_2\text{Si}=\text{CH}_2$  can be produced. Then, in step (iii), as  $\text{SiH}_2$  reacts readily with  $\text{HSiCH}_3$ , molecular  $\text{SiH}_4$  can finally be regenerated. Since the formation of  $\text{HSiCH}_3$  is dominant at temperatures below  $700^\circ\text{C}$  and the  $\text{H}_2\text{Si}=\text{CH}_2$  formation is relatively minor,  $\text{SiCH}_4$  is needed as the main radical for C incorporation since it can diffuse across the surface of H-covered sites such as  $\text{SiH}_2$  and can be inserted into Si-H or C-H surface bonds.<sup>29,30</sup> Hence, step (iii) is decisive for the incorporation of C in  $\text{Si}_{1-x}\text{C}_x$  films by forming  $\text{SiCH}_4$  radicals. Yet, for  $\text{Si}_{1-x}\text{C}_x$  NWs, the growth mechanism by the VLS method using a Au catalyst has not been studied extensively until now. Some groups have simply pronounced the growth of C materials, such as single-wall or multi-wall carbon nanotubes and carbon nanowires. They have demonstrated that the growth of C materials generally proceeds *via* the VLS mechanism, like Si NWs, based on the reaction process involving C uptake, supersaturation, and precipitation in an iron-group catalyst.<sup>31–33</sup> In addition, it has recently been reported that C materials can be grown by the VLS method using very small Au particles (about 5–30 nm) in the role of the catalyst because the solubility of C is enhanced in nano-sized Au catalysts; it was a new discovery in the field of nanoscience because actually, unlike nano-size Au particles, the solubility of C in bulk-phase Au is extremely low.<sup>34–37</sup> Based on the above-mentioned thermal decomposition process in  $\text{Si}_{1-x}\text{C}_x$  films, we expected that  $\text{Si}_{1-x}\text{C}_x$  NWs would be grown with substitutionally incorporated C atoms by intact Si-C bonds in the wire. For this process to occur, the  $\text{SiH}_4$  and  $\text{CH}_3\text{SiH}_3$  gases would have to be simultaneously adsorbed on the Au catalyst and dissolved in droplets (liquid phase); the droplets would then become supersaturated through the dissolving process. Finally,  $\text{Si}_{1-x}\text{C}_x$  NWs would be precipitated from the supersaturated catalyst. However, the  $\text{Si}_{1-x}\text{C}_x$  NWs grown in our system did not

contain any substitutionally incorporated C atoms (Si–C bonds), despite the high quantity of C in the wire. From the perspective of the growth kinetics of C materials, C atoms are incorporated into the catalyst through the decomposition of C-bearing molecules on the catalyst surface. This process suggests that the absence of substitutionally incorporated C atoms is due to the cleavage of Si–C bonds in  $\text{CH}_3\text{SiH}_3$  compounds ( $\text{CH}_3\text{SiH}_3(\text{g}) \rightarrow \text{SiH}_3 + \text{CH}_3$ ) on the Au catalyst – the products of which are then dissolved in the liquid state Au droplets.<sup>35,36</sup> Furthermore, the breaking of Si–C bonds in  $\text{CH}_3\text{SiH}_3$  inhibits the reaction process of (iii), resulting in no production of the  $\text{SiCH}_4$  radicals required for C incorporation. Hence, the fact that Si–C bonding was not detected in the FT-IR and Raman spectra can be attributed to the decomposition of C-bearing molecules through the Au catalyst in the liquid state. Possible decomposition pathways of the gas phase reaction of  $\text{SiH}_4$  with  $\text{CH}_3\text{SiH}_3$  are described in Fig. 3 for both film growth without Au and wire growth with an Au catalyst. We performed fitting of C 1s core-level spectra to verify the formation process and chemical state of the interstitial C for the above-mentioned argument. Fig. 4 showed the C 1s spectra as a function of the  $\text{CH}_3\text{SiH}_3$  gas content, which was fitted by the electronegativity values contributing to the chemical states. The C 1s peak of the as-grown Si NWs contained only C–C bonds from surface contamination. As the  $\text{CH}_3\text{SiH}_3$  gas content increased, two states emerged at 282.2 eV and 286 eV. Previously reported results have shown that the peak position between 282.4 and 283 eV is caused by Si–C bonding, and the intensity is proportional to the quantity of C content in the film.<sup>26,27</sup> However, in our case, the peak at 282.2 eV was observed at a lower binding energy than that for Si–C bonding, and this chemical state has not yet been reported in XPS spectra. We suggest that the peak of 282.2 eV could be induced by the interstitial incorporation of C atoms because interstitially incorporated atoms are generally located as elemental atoms at a lower binding energy than bulk-like bonds; *i.e.*, we were able to verify the existence of interstitial C atoms in the wire from the fitted results.<sup>18,38</sup> On the other hand, the peak at 286 eV is likely related to the Si–O–C bonding induced by the surface contamination with a native oxide. After the sputtering process, these

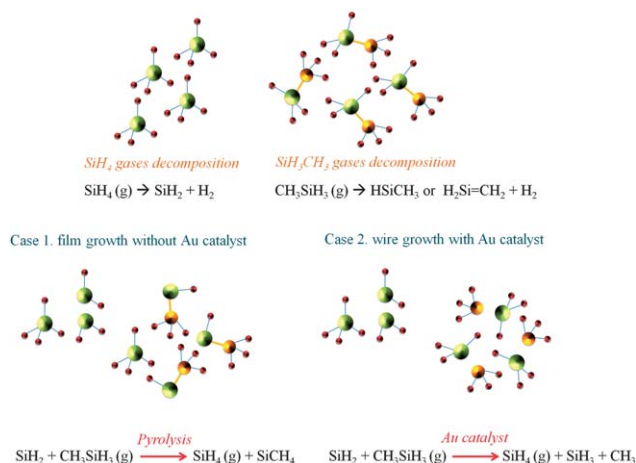


**Fig. 3** A schematic diagram of possible decomposition pathways in the gas phase reactions of  $\text{SiH}_4$  with  $\text{CH}_3\text{SiH}_3$ , for both film growth without Au and wire growth with a Au catalyst.

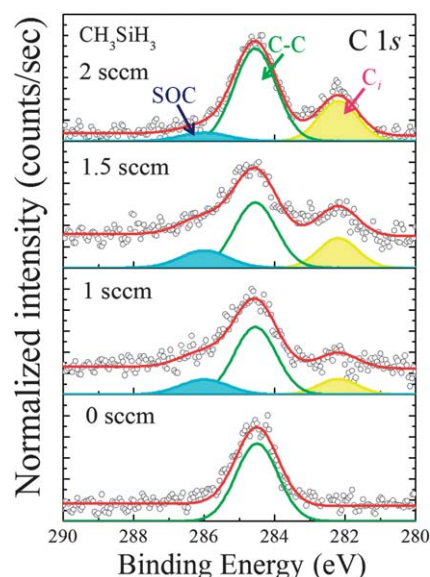


**Fig. 4** The core-level spectra of C 1s obtained from the  $\text{Si}_{1-x}\text{C}_x$  NWs depending on  $\text{CH}_3\text{SiH}_3$  gas flow rate. The peak of C atoms ( $\text{C}_i$ ) interstitially incorporated in the Si pillar increased in proportion to the  $\text{CH}_3\text{SiH}_3$  gas content.

Si–O–C states completely disappeared.<sup>25</sup> Thus, in summary,  $\text{Si}_{1-x}\text{C}_x$  NWs can be grown by the VLS method when  $\text{CH}_3\text{SiH}_3$  gas is injected into the Au catalyst along with  $\text{SiH}_4$  gas, thereby overcoming the extremely low C solubility in Au and resulting in the interstitial incorporation of a high number of C atoms.

Next, we investigated the optical properties of  $\text{Si}_{1-x}\text{C}_x$  NWs as a function of the interstitial C atoms and a large number of Au nanoparticles along the sidewall of the wire. We focused on the characteristics of Au nanoparticles since light absorption by surface plasmons of metallic nanoparticles is considered to be an important feature for optical devices. The reflectance spectra of a Si wafer and  $\text{Si}_{1-x}\text{C}_x$  NWs as a function of the  $\text{CH}_3\text{SiH}_3$  gas content are shown in ESI Fig. S6.† Because of the high refractive index of the bare Si wafer, which is mirror-like and single crystalline, the Si substrate produced a high reflectance. In contrast, the reflectance of  $\text{Si}_{1-x}\text{C}_x$  NWs decreased overall and a particularly deeply curved shape was observed near 500 nm. To determine the optical conductivity ( $\sigma$ ), we simulated the reflectance spectra of  $\text{Si}_{1-x}\text{C}_x$  NWs as a function of the C content using the program “Reffit” by A.B. Kuzmenko.<sup>39</sup> Here,  $\sigma(\omega)$  was derived from the equation given by

$$\sigma(\omega) = \frac{\omega_p^2}{4\pi} \frac{i}{\omega + i\Gamma}$$

where  $\omega_p$  and  $\Gamma$  are the plasma frequency and carrier scattering rate of  $1/\tau$ , respectively. The real part of  $\sigma(\omega)$  was extracted from the fitted results and is described in Fig. 5. From the results, we verified the surface plasmon effect from the Au nanoparticles on the sidewall and  $\text{CH}_3\text{SiH}_3$  gas; for 1.5 sccm of  $\text{CH}_3\text{SiH}_3$ , the SPR peak was clearly visible at 500 nm, and for 2 sccm of  $\text{CH}_3\text{SiH}_3$ , it was red-shifted with the broadening of the bandwidth. Conversely, noticeable SPR peaks were not observed for the  $\text{CH}_3\text{SiH}_3$  flow rates of 0 and 1 sccm. To better understand the SPR phenomenon, we investigated the Au 4f core level and

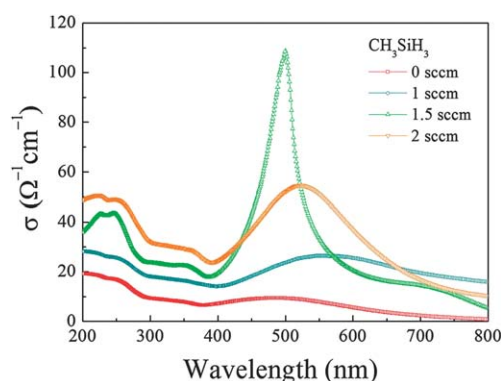


**Fig. 5** Optical conductivity ( $\sigma$ ) spectra simulated from the reflectance spectra of  $\text{Si}_{1-x}\text{C}_x$  NWs as a function of the C content using the Refit program.

valence band spectra, which provide information on the chemical states and charge distribution at the Fermi edge of the  $\text{Si}_{1-x}\text{C}_x$  NWs as a function of the  $\text{CH}_3\text{SiH}_3$  gas content. Note that Au 4f spectra only contain information on the chemical states of the Au nanoparticles located along the exterior, not the interior, of the wire since XPS is well known to be surface sensitive. Nevertheless, the Au 4f spectra first indicated entire peak shift toward higher binding energy with increasing  $\text{CH}_3\text{SiH}_3$  gas content, as shown in Fig. 6(e). This shift, in addition to the peak broadening of the Au 4f spectra, indicates the formation of another chemical phase interacting with the Au atoms, which can be directly related to the deformed Au tip shape, as indicated in Fig. 6(a)–(d). We fitted the Au 4f spectra based on the electronegativity values of Si (1.9) and C (2.5), given that Si has a weaker grip on its outer shell electron than C. Therefore, the three peaks in the Au 4f spectra were assigned as follows: Au–Au ( $\sim 84$  eV), Au–Si ( $\sim 85$  eV), and Au–C ( $\sim 86$  eV). From the fitting results, the entire

peak shift of Au 4f as a function of the  $\text{CH}_3\text{SiH}_3$  gas content was induced by a rise in the Si and C quantities that were incorporated in Au. Consequently, the Au–Si and Au–C states grew increasingly larger, as shown in Fig. 6(e). The incorporation of Si and C in Au is closely correlated with the Au nanoparticles along the sidewall, not the bulk-like Au tip at top of the wire, considering the extremely low solubility of Si and C in Au at room temperature. In particular, in small Au particles (*i.e.*, sizes of  $\sim 5$  nm or smaller in reported data), the C solubility in Au should increase drastically and the driving force of C precipitation from Au should be suppressed,<sup>35</sup> thereby allowing the Au nanoparticles along the sidewall to react with the number of C atoms interstitially incorporated in the wire due to the high injection of  $\text{CH}_3\text{SiH}_3$  gas. The occurrence of this phenomenon was evident from the Au–C bond, as shown in Fig. 6(e). The increase of the Au–Si bonding, which stood in stark contrast to the decrease of the Au–Au bonding, can be attributed to the formation of an Au-silicide phase in nanoparticles of Au in contact with the Si pillar. Namely, the metamorphosed shape of the Au tip was intensified in proportion to the  $\text{CH}_3\text{SiH}_3$  gas content because the Au diffusion along the sidewall of the wire increased. A substantial number of Au nanoparticles formed by diffused Au atoms absorbed the light until the  $\text{CH}_3\text{SiH}_3$  content reached 1.5 sccm, resulting in the SPR effect. However, once the  $\text{CH}_3\text{SiH}_3$  content reached 2 sccm, the peak position, width, and intensity of SPR changed (Fig. 5). The red-shifted and broadened SPR peak was due to the excitation of different oscillations, not the coherent oscillation of the intrinsic Au nanoparticles.<sup>14</sup> This change can be explained by a rise of the Au–C bond, as confirmed by the Au 4f fitting results, which generated different oscillations from the Au nanoparticles, resulting in SPR broadening. On the other hand, according to previously published results, a change in the SPR position depends on the Au particle size, suggesting that a red shift of the SPR peak could be a response to coarsening of the Au nanoparticles in the twisted region compared to the Au

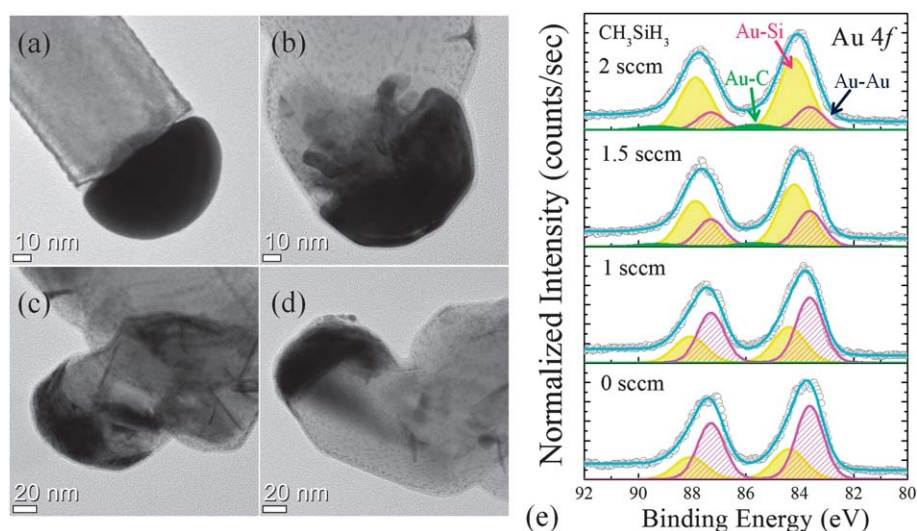


**Fig. 6** TEM images of a deformed Au tip in  $\text{Si}_{1-x}\text{C}_x$  NWs grown as a function of flow rate ratio of  $\text{SiH}_4$  to  $\text{CH}_3\text{SiH}_3$  gas. (a) As-grown Si NWs, exhibiting a complete hemisphere.  $\text{Si}_{1-x}\text{C}_x$  NWs with a deformed Au tip and a  $\text{SiH}_4$  to  $\text{CH}_3\text{SiH}_3$  gas flow ratio of (b) 10 to 1 sccm, (c) 10 to 1.5 sccm, and (d) 10 to 2 sccm. (e) Fitting results of Au 4f core-level spectra. The peak of the Au–C bond in Au nanoparticles on the sidewall of the wire is noticeably present in the case of 2 sccm of  $\text{CH}_3\text{SiH}_3$  gas.



nanoparticles along the flat sidewall.<sup>14,40</sup> The decrease in the SPR intensity can also be associated with the small surface area when incident light strikes the  $\text{Si}_{1-x}\text{C}_x$  NWs; in the case of  $\text{CH}_3\text{SiH}_3$  2 sccm, although the C content in the Au nanoparticles was higher, the total length was shorter and the diameter was similar compared to the case of 1.5 sccm  $\text{CH}_3\text{SiH}_3$ .

Moreover, since the distribution of the occupied state is closely related to the optical process, it was necessary to probe the electron distribution of the occupied energy state; thus, the valence band spectra were analyzed as a function of the  $\text{CH}_3\text{SiH}_3$  gas content, as shown in Fig. 7. For the  $\text{Si}_{1-x}\text{C}_x$  NWs, the valence band was determined by the Au s-band and d-band; the former appears as a Fermi edge at zero binding energy while the latter dominates below  $\sim 2$  eV because of high population and cross-section.<sup>41</sup> The spin-orbit splitting ( $\Delta_{5d}$ ), as clearly presented in Fig. 7, reflects the Au–Au d–d interaction and became narrower as the coordination number of the nearest Au atom decreased.<sup>42,43</sup> Thus, the  $\Delta_{5d}$  of Au nanoparticles should be narrower due to the reduction in the coordination number of the nearest Au neighbor relative to the Au bulk (generally,  $\Delta_{5d} \approx 2.6$  eV), which is reasonably consistent with our results ( $\Delta_{5d}$ : 2.35–2.02 eV).<sup>41</sup> Moreover, it is interesting to note that there is a clearly visible discrepancy in the  $\Delta_{5d}$  values – i.e.,  $\Delta_{5d}$  decreased more for higher values of the  $\text{CH}_3\text{SiH}_3$  gas content. These diminishing  $\Delta_{5d}$  values were observed when the density of Au atoms in the nanoparticles was diluted in alloy formation, which causes a moving away of the top of the d-band from the Fermi edge. This observation is clearly in accordance with the behavior of the SPR and Au 4f fitting results. In other words, in Au nanoparticles, the formation of Au–C bonds with increasing  $\text{CH}_3\text{SiH}_3$  gas content gives rise to a reduction in the coordination number of the nearest Au neighbors, which causes the  $\Delta_{5d}$  values to become narrower. Furthermore, the number of Au nanoparticles on the sidewall was regulated by the diffusion of the Au catalyst at the tip with increasing  $\text{CH}_3\text{SiH}_3$  gas and induced the SPR effect. Thus, SPR characteristics can be modified by exploiting the Au–C bonds formed in the Au nanoparticles since interactions between Au and C atoms can induce oscillations that differ from those of the intrinsic Au nanoparticles.

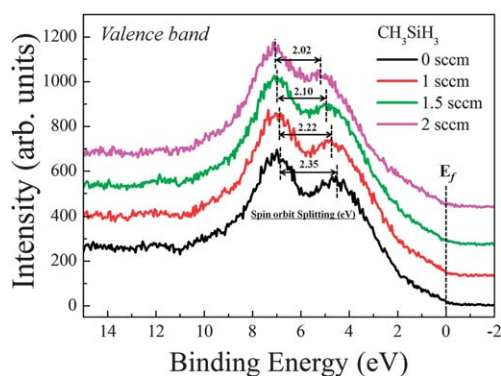


**Fig. 7** Valence band spectra of the  $\text{Si}_{1-x}\text{C}_x$  NWs as a function of the  $\text{CH}_3\text{SiH}_3$  gas content. As the gas content increased, the spin-orbit splitting ( $\Delta_{5d}$ , Au–Au d–d interaction) became narrower.

## IV. Conclusion

In this study, we systematically analyzed the interaction between Au and C atoms in two cases – one where the Au catalyst was located at the top of the wire, and the other where Au nanoparticles were distributed along the sidewalls of  $\text{Si}_{1-x}\text{C}_x$  NWs. The  $\text{Si}_{1-x}\text{C}_x$  NWs were grown using the VLS method with a Au catalyst and simultaneous injections of  $\text{SiH}_4$  and  $\text{CH}_3\text{SiH}_3$ . However, C atoms were interstitially – not substitutionally – incorporated into the Si structure because Si–C bonding was separated through the Au catalyst (Au–Si liquid state). On the other hand, we detected numerous Au nanoparticles on the sidewall formed by the diffusion of the Au catalyst in  $\text{Si}_{1-x}\text{C}_x$  NWs, which was enhanced with the increase in  $\text{CH}_3\text{SiH}_3$  gas content. In particular, we observed a sharp surface plasmon absorption peak when the  $\text{CH}_3\text{SiH}_3$  gas flow rate increased more than 1.5 sccm. Additionally, the plasmon absorption peak changed its width, intensity and position for the  $\text{CH}_3\text{SiH}_3$  gas flow rate of 2 sccm, which was a response to the existence of Au–C bonds, as verified by the Au 4f fitting results and valence band spectra. Hence, the change in Au nanoparticles caused by the formation of Au–C bonds can directly affect the modulation of the SPR.

## Acknowledgements

This work was partially supported by the New and Renewable Energy R&D program (Grant no. 2009T100100614) under the Ministry of Knowledge Economy, Republic of Korea, as well as a grant from the Seoul Science Fellowship of the Seoul Metropolitan Government.

## References

- P. Boucaud, C. Francis, A. Larre, F. H. Julien, J.-M. Lourtioz, D. Bouchier, S. Bodnar and J. L. Regolini, Photoluminescence of strained  $\text{Si}_{1-y}\text{C}_y$  alloys grown at low temperature, *Appl. Phys. Lett.*, 1995, **66**, 70.
- J. L. Regolini, S. Bodnar, J. C. Oberlin, F. Ferrieu, M. Gauneau, B. Lambert and P. Boucaud, Strain compensated heterostructures in the  $\text{Si}_{1-x-y}\text{Ge}_x\text{C}_y$  ternary system, *J. Vac. Sci. Technol., A*, 1994, **12**, 1015.
- R. W. Olesinski and G. J. Abbaschian, The C–Si (Carbon–Silicon) system, *Bull. Alloy Phase Diagrams*, 1984, **5**, 486.
- R. C. Henderson and R. F. Helm, Silicon homoepitaxial thin films via silane pyrolysis: a HEED and Auger electron spectroscopy study, *Surf. Sci.*, 1972, **30**, 310.
- J. B. Posthill, R. A. Rudder, S. V. Hattangady, G. G. Fountain and R. J. Markunas, On the feasibility of growing dilute  $\text{C}_x\text{Si}_{1-x}$  epitaxial alloys, *Appl. Phys. Lett.*, 1990, **56**, 734.
- S. Zerlauth, H. Seyringer, C. Penn and F. Schaffler, Growth conditions for complete substitutional carbon incorporation into  $\text{Si}_{1-y}\text{C}_y$  layers grown by molecular beam epitaxy, *Appl. Phys. Lett.*, 1997, **71**, 3826.
- S. Y. Park, J. D'Arcy-Gall, D. Gall, J. A. N. T. Soares, Y.-W. Kim, H. Kim, P. Desjardins, S. G. Bishop and J. E. Greene, Carbon incorporation pathways and lattice sites in  $\text{Si}_{1-y}\text{C}_y$  alloys grown on Si(001) by molecular-beam epitaxy, *J. Appl. Phys.*, 2002, **91**, 5716.
- Y. L. Foo, K. A. Bratland, B. Cho, P. Desjardins and J. E. Greene,  $\text{Si}_{1-y}\text{C}_y/\text{Si}(100)$  gas-source molecular beam epitaxy from  $\text{Si}_2\text{H}_6$  and  $\text{CH}_3\text{SiH}_3$ : surface reaction paths and growth kinetics, *J. Appl. Phys.*, 2003, **93**, 3944.
- T. O. Mitchell, J. L. Hoyt and J. F. Gibbons, Substitutional carbon incorporation in epitaxial  $\text{Si}_{1-y}\text{C}_y$  layers grown by chemical vapor deposition, *Appl. Phys. Lett.*, 1997, **71**, 1688.

- 10 S. K. Ray, D. W. McNeill, D. L. Gay, C. K. Maiti, G. A. Armstrong, B. M. Armstrong and H. S. Gamble, Comparison of  $\text{Si}_{1-y}\text{C}_y$  films produced by solid-phase epitaxy and rapid thermal chemical vapour deposition, *Thin Solid Films*, 1997, **294**, 149.
- 11 A. C. Mocuta and D. W. Greve, Epitaxial  $\text{Si}_{1-y}\text{C}_y$  alloys: the role of surface and gas phase reactions, *J. Appl. Phys.*, 1999, **85**, 1240.
- 12 Y. L. Foo, K. A. Bratland, B. Cho, J. A. N. T. Soares, P. Desjardins and J. E. Greene, C incorporation and segregation during  $\text{Si}_{1-y}\text{C}_y/\text{Si}(001)$  gas-source molecular beam epitaxy from  $\text{Si}_2\text{H}_6$  and  $\text{CH}_3\text{SiH}_3$ , *Surf. Sci.*, 2002, **513**, 475.
- 13 D. Chandrasekhar, J. McMurran, D. J. Smith, J. D. Lorentzen, J. Menendez and J. Kouvetakis, Strategies for the synthesis of highly concentrated  $\text{Si}_{1-y}\text{C}_y$  diamond-structure system, *Appl. Phys. Lett.*, 1998, **72**, 2117.
- 14 S. Link and M. A. El-Sayed, Spectral properties and relaxation dynamics of surface plasmon electronic oscillations in gold and silver nanodots and nanorods, *J. Phys. Chem. B*, 1999, **103**, 8410.
- 15 Y. Tian and T. Tatsuma, Mechanisms and applications of plasmon-induced charge separation at  $\text{TiO}_2$  films loaded with gold nanoparticles, *J. Am. Chem. Soc.*, 2005, **127**, 7632.
- 16 W. Haiss, N. T. K. Thanh, J. Aveyard and D. G. Fernig, Determination of size and concentration of gold nanoparticles from UV-vis spectra, *Anal. Chem.*, 2007, **79**, 4215.
- 17 W. J. Lee, J. W. Ma, J. M. Bae, M. H. Cho and J. P. Ahn, Effects of hydrogen on Au migration and the growth kinetics of Si nanowires, *CrystEngComm*, 2011, **13**, 690.
- 18 W. J. Lee, J. W. Ma, J. M. Bae, S. H. Park, M. H. Cho and J. P. Ahn, The modulation of  $\text{Si}_{1-x}\text{Ge}_x$  nanowires by correlation of inlet gas ratio with  $\text{H}_2$  gas content, *CrystEngComm*, 2011, **13**, 5204.
- 19 C. B. Collins, R. O. Carlson and C. J. Gallagher, Properties of gold-doped silicon, *Phys. Rev.*, 1957, **105**, 1168.
- 20 S. S. Lyer, K. Eberl, M. S. Goorsky, F. K. LeGoues, J. C. Tsang and F. Cardone, Synthesis of  $\text{Si}_{1-y}\text{C}_y$  alloys by molecular beam epitaxy, *Appl. Phys. Lett.*, 1992, **60**, 356.
- 21 T. Chengchun, B. Yoshio, S. Tadao and K. Keiji, Uniform boron nitride coatings on silicon carbide nanowires, *Adv. Mater.*, 2002, **14**, 1046.
- 22 X. D. Han, Y. F. Zhang, K. Zheng, X. N. Zhang, Y. J. Hao, X. Y. Guo, J. Yuan and Z. L. Wang, Low-temperature *in situ* large strain plasticity of ceramic SiC nanowires and its atomic-scale mechanism, *Nano Lett.*, 2007, **7**, 452.
- 23 H. W. Shim and H. Huang, Three-stage transition during silicon carbide nanowire growth, *Appl. Phys. Lett.*, 2007, **90**, 083106.
- 24 S. Perisanu, P. Vincent, A. Ayari, M. Choueib, S. T. Purcell, M. Bechelany and D. Cornu, High Q factor for mechanical resonances of batch-fabricated SiC nanowires, *Appl. Phys. Lett.*, 2007, **90**, 043113.
- 25 Y. S. Tan, S. Y. M. Chooi, C. Y. Sin, P. Y. Ee, M. P. Srinivasan and S. O. Pehkonen, Characterization of low-k dielectric trench surface cleaning after a fluorocarbon etch, *Thin Solid Films*, 2004, **462**, 250.
- 26 G. Raciukaitis, M. Brikas, V. Kazlauskienė and J. Miskinis, Doping of silicon with carbon during laser ablation process, *Appl. Phys. A: Mater. Sci. Process.*, 2006, **85**, 445.
- 27 H. J. Osten, M. Methfessel, G. Lippert and H. Rucker, Observation of the formation of a carbon-rich surface layer in silicon, *Phys. Rev. B: Condens. Matter Mater. Phys.*, 1995, **52**, 12179.
- 28 E. Inger, W. Erik, C. Dan, O. Hakan and O. Eva, Preparation and characterization of electrochemically etched W tips for STM, *Meas. Sci. Technol.*, 1999, **10**, 11.
- 29 A. D. Johnson, J. Perrin, J. A. Mucha and D. E. Ibbotson, Kinetics of SiC CVD: surface decomposition of silacyclobutane and methylsilane, *J. Phys. Chem.*, 1993, **97**, 12937.
- 30 J. Mi, P. Warren, M. Gailhanou, J.-D. Ganiere, M. Duatoit, P.-H. Jouneau and R. Houriet, Epitaxial growth of  $\text{Si}_{1-x-y}\text{Ge}_x\text{C}_y$  alloy layers on (100) Si by rapid thermal chemical vapor deposition using methylsilane, *J. Vac. Sci. Technol., B: Microelectron. Nanometer Struct.-Process., Meas., Phenom.*, 1996, **14**, 1660.
- 31 Y. Shibuta and S. Maruyama, Molecular dynamics simulation of formation process of single-walled carbon nanotubes by CCVD method, *Chem. Phys. Lett.*, 2003, **382**, 381.
- 32 D. Feng and B. Kim, The importance of supersaturated carbon concentration and its distribution in catalytic particle for single-walled carbon nanotube nucleation, *Nanotechnology*, 2006, **17**, 543.
- 33 A. R. Harutyunyan, E. Mora, T. Tokune, K. Bolton, A. Rosen, A. Jiang, N. Awasthi and S. Curtarolo, Hidden features of the catalyst nanoparticles favorable for single-walled carbon nanotube growth, *Appl. Phys. Lett.*, 2007, **90**, 163120.
- 34 S. Bhaviripudi, E. Mile, S. A. Steiner III, A. T. Zare, M. S. Dresselhaus, A. M. Belcher and J. Kong, CVD synthesis of single-walled carbon nanotubes from gold nanoparticle catalysts, *J. Am. Chem. Soc.*, 2007, **129**, 1516.
- 35 D. Takagi, Y. Kobayashi, H. Hibino, S. Suzuki and Y. Homma, Mechanism of gold-catalyzed carbon material growth, *Nano Lett.*, 2008, **8**, 832.
- 36 D. Takagi, Y. Homma, H. Hibino, S. Suzuki and Y. Kobayashi, Single-walled carbon nanotube growth from highly activated metal nanoparticles, *Nano Lett.*, 2006, **6**, 2642.
- 37 H. Okamoto and T. B. Massalski, The Au-C (Gold-Carbon) system, *Bull. Alloy Phase Diagrams*, 1984, **5**, 378.
- 38 B. Brennan and G. Hughes, Identification and thermal stability of the native oxides on InGaAs using synchrotron radiation based photoemission, *J. Appl. Phys.*, 2010, **108**, 053516.
- 39 A. B. Kuzmenko, Kramers-Kronig constrained variational analysis of optical spectra, *Rev. Sci. Instrum.*, 2005, **76**, 083108.
- 40 H. Liao, W. Wen and G. K. L. Wong, Photoluminescence from Au nanoparticles embedded in Au:oxide composite films, *J. Opt. Soc. Am. B*, 2006, **23**, 2518.
- 41 P. Zhang and T. K. Sham, X-ray studies of structure and electronic behavior of alkanethiolate-capped gold nanoparticles: the interplay of size and surface effects, *Phys. Rev. Lett.*, 2003, **90**, 245502.
- 42 T. K. Sham, Y. M. Yiu, M. Kuhn and K. H. Tan, Electron structure of ordered and disordered  $\text{Cu}_3\text{Au}$ : the behavior of the Au 5d bands, *Phys. Rev. B: Condens. Matter Mater. Phys.*, 1990, **41**, 11881.
- 43 A. Bzowski, T. K. Sham, R. E. Watson and M. Weinert, Electron structure of Au and Ag overlayers on Ru(001): the behavior of the noble-metal d bands, *Phys. Rev. B: Condens. Matter Mater. Phys.*, 1995, **51**, 9979.